

1 **From Precipitation to Prediction: Integrating**
2 **ConvLSTM Models for Comprehensive River Runoff**
3 **Forecasting**

4 **Florian Börgel¹, Sven Karsten¹, Karoline Rummel¹**

5 ¹Leibniz-Institute for Baltic Sea Research Warnemünde,

6 **Abstract**
 7 a

8 **Plain Language Summary**
 9 b

10 **1 Introduction**

11 River runoff is an important component of the global water cycle as it comprises
 12 about one third of the precipitation over land areas (Hagemann et al., 2020). In
 13 the context of climate change studies, river runoff is usually generated in two ways.
 14 First, river runoff as input for ocean models can be created using hydrological mod-
 15 els such as the Hydrological Discharge (HD) model (Hagemann et al., 2020). HD
 16 models calculates the water balance using hydrological processes (e.g. snow, glaciers,
 17 soil moisture, groundwater contribution). It represents a complex forecasting tool
 18 that uses underlying physical processes. A different approach would use data-based
 19 models that integrate statistical correction, using the land surface schemes of global
 20 or regional climate models.

21 The relatively recent emergence of machine learning (ML) models has offered differ-
 22 ent approaches to river runoff forecasting. Accurate runoff forecasting is crucial for
 23 effective water resources management, particularly over extended periods (W. Fang
 24 et al., 2019; Tan et al., 2018). Common approaches employ feed-forward artificial
 25 neural networks, support vector machines, adaptive neuro-fuzzy inference systems,
 26 and notably, Long Short-Term Memory (LSTM) neural networks that have gained
 27 traction for long-term hydrological forecasting due to their excellent performance
 28 (Ashrafi et al., 2017; L. Fang & Shao, 2022; Huang et al., 2014; Humphrey et al.,
 29 2016; Kratzert et al., 2018; Liu et al., 2020).

30 LSTM networks, first introduced by Hochreiter & Schmidhuber (1997) , are an evo-
 31 lution of the classical Recurrent Neural Networks (RNNs). Their structure enables
 32 them to learn long-term dependencies while avoiding the vanishing or exploding
 33 gradient problem. They have shown stability and efficacy in sequence-to-sequence
 34 predictions. However, a limitation of LSTMs is their inability to effectively capture
 35 two-dimensional structures, an area where Convolutional Neural Networks (CNNs)
 36 excel. Recognizing this limitation SHI et al. (2015) proposed a Convolutional LSTM
 37 (ConvLSTM) architecture, which combines the strengths of both LSTM and CNN.
 38 The ConvLSTM network has been proven useful for spatio-temporal applications
 39 such as precipitation nowcasting (SHI et al., 2015), flood forecasting (Moishin et al.,
 40 2021), and river runoff forecasting (Ha et al., 2021; Zhu et al., 2023).

41 In this work, we demonstrate that ConvLSTM networks are a reliable method for
 42 predicting multiple rivers simultaneously, using only atmospheric forcing, even in
 43 the absence of a fully functional hydrological model with a complex parameteriza-
 44 tion. We use the Baltic Sea catchment as an example to illustrate our approach.
 45 Although the methodology we propose is universally applicable across various geo-
 46 graphic regions, the Baltic Sea presents a challenge due to its unique hydrological
 47 characteristics, being nearly decoupled from the open ocean (see Figure). As a con-
 48 sequence, the salinity of the Baltic Sea is driven to a large part by freshwater supply
 49 from rivers. Freshwater enters the Baltic Sea through river runoff or positive net
 50 precipitation (precipitation minus evaporation) over the sea surface. The net precip-
 51 itation accounts for 11 % and the river input for 89 % of the total freshwater input
 52 (Meier & Döscher, 2002). Modelling the Baltic Sea is therefore to a large part the
 53 result of the quality of the river input, that is used for the simulation. This makes
 54 the accurate modeling of river runoff especially critical for simulations pertaining to
 55 the Baltic Sea.

56 In this work we will, we present a ConvLSTM architecture that is able to predict
 57 daily river runoff for 97 rivers across the Baltic Sea catchment. ***mehr Fokus auf***
 58 ***Neues?***

59 **2 Methods**

60 **2.1 Runoff data used for training**

61 The runoff data covering the period 1979 to 2011 is based on an E-HYPE hindcast
 62 simulation that was forced by a regional downscaling of ERA-Interim (Dee et al.,
 63 2011) with RCA3 (“The rossby centre regional climate model RCA3,” n.d.) and im-
 64 plemented into NEMO-Nordic (Hordoir et al., 2019) as a mass flux. For the periods
 65 before (1961 to 1978) and after (2012 to 2018) additional spatial temporal correc-
 66 tions have been applied to the runoff data, and have therefore been ignored. For
 67 more information see Gröger et al. (2022) and references therein.

68 **2.2 Atmospheric Forcing**

69 The UERRA-HARMONIE regional reanalysis dataset was developed as part of
 70 the FP7 UERRA project (Uncertainties in Ensembles of Regional Re-Analyses,
 71 <http://www.uerra.eu/>,). The UERRA-HARMONIE system represents a comprehen-
 72 sive, high-resolution reanalysis covering a wide range of essential climate variables.
 73 This dataset encompasses data on air temperature, pressure, humidity, wind speed
 74 and direction, cloud cover, precipitation, albedo, surface heat fluxes, and radiation
 75 fluxes from January 1961 to July 2019. With a horizontal resolution of 11 km and
 76 analyses conducted at 00 UTC, 06 UTC, 12 UTC, and 18 UTC, it also provides
 77 hourly resolution forecast model data. UERRA-HARMONIE is accessible through
 78 the Copernicus Climate Data Store (CDS, <https://cds.climate.copernicus.eu/#!/home>), initially produced during the UERRA project and later transitioned to
 79 the Copernicus Climate Change Service (C3S, <https://climate.copernicus.eu/copernicus-regionalreanalysis-europe>).
 80

81 **2.3 Ocean Model**

82 To simulate the Baltic Sea, we use a coupled 3-dimensional ocean model Baltic Sea,
 83 called the Modular Ocean Model (MOM). This model uses a finite-difference method
 84 to solve the full set of primitive equations to calculate the motion of water and the
 85 transport of heat and salt. The K-profile parameterization (KPP) was used as tur-
 86 bulence closure scheme. The model’s western boundary opens into the Skagerrak
 87 and connects the Baltic Sea to the North Sea. The maximum depth was set at 264
 88 meters. A more detailed description of the setup can be found in (Gröger et al.,
 89 2022).

90 **2.4 LSTM network**

91 Before turning to the convolutional LSTM, the simpler architecture of the plain
 92 LSTM is examined and should serve as a role model for the later consideration of
 93 the full ConvLSTM.

94 The Long Short-Term Memory (LSTM), a specialized form of Recurrent Neu-
 95 ral Networks (RNNs), is specifically tailored for modeling temporal sequences
 96 $\vec{X}^t[1], \dots \vec{X}^t[\tau], \dots \vec{X}^t[N_\tau]$ of N_τ input quantities $\vec{X}^t[\tau] = (X_{k,\tau}^t) \in \mathbb{R}^{N_k}$. The se-
 97 quence is taken from a dataset given in form of a time series $\{\vec{X}^t\}$ and the endpoint
 98 should coincide with the specific element in the time series connected to time t ,
 99 i.e. $\vec{X}^t[N_\tau] \equiv \vec{X}^t$. The N_k is the number of used input “channels” and can, for exam-
 100 ple, represent different measurable quantities. Its unique design allows it to adeptly
 101 handle long-range dependencies, setting it apart from traditional RNNs in terms of
 102 accuracy (see Figure 1).

103 This performance in modeling long-range dependencies has been validated in
 104 various studies. The key component of LSTM’s innovation is its memory cell,
 105 $\vec{C}^t[\tau] = (C_h^t[\tau]) \in \mathbb{R}^{N_h}$, which stores state information, also referred to as long-

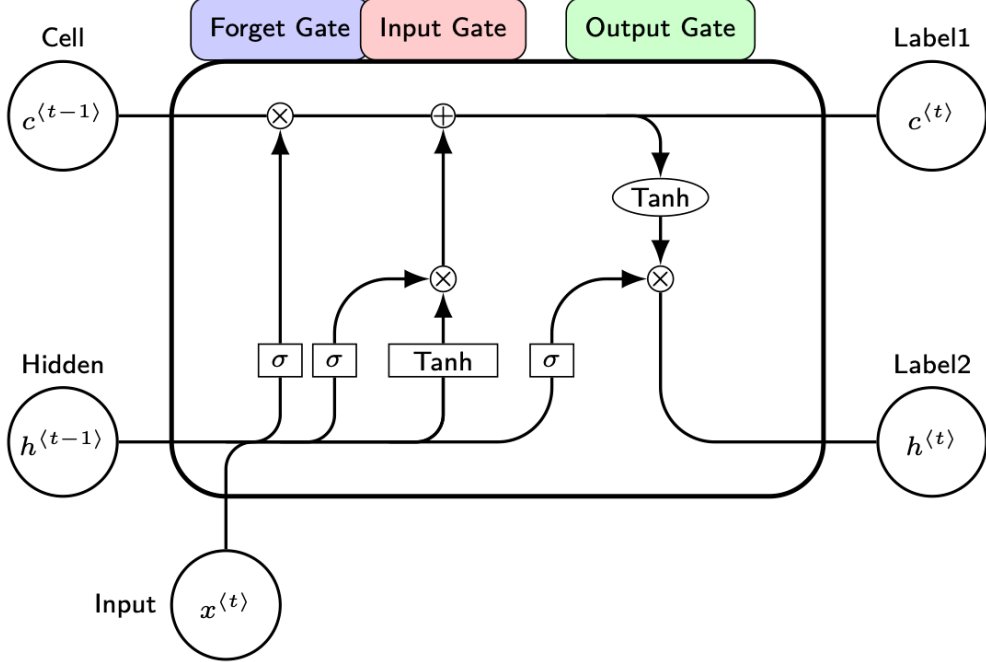


Figure 1: Inner structure of a Long Short-Term Memory Cell

term memory. The index $\tau \in [1, N_\tau]$ corresponds to the τ -th element in the input sequence. The cell state is a vector consists of elements, each associated with one of the N_h hidden layers, labeled by h . This vector is determined through several self-parameterized gates, all in the same vector space as $\vec{C}^t[\tau]$. The forget gate $\vec{F}^t[\tau]$ defines the percentage of the previous long-term memory status $\vec{C}^t[\tau-1]$ that should be retained stored. The input gate $\vec{I}^t[\tau]$ decides how much of the input is added to the the long-term memory, forming the updated cell state. The so-called output gate $\vec{O}^t[\tau]$ then determines how much of the latest cell output, $\vec{C}^t[\tau]$, is propagated to the final state, $\vec{H}^t[\tau]$ representing the updated short-term memory of the hidden state.

For a fixed point τ in the sequence, the action of a LSTM cell, i.e. the connection between the input $\vec{X}^t[\tau]$, the various gates and the state vectors, is given as follows. First, the elements of the input sequence together with the hidden state are mapped onto auxiliary gate vectors, collectively denoted by $\vec{g}^t[\tau] = (g_h^t[\tau]) \in \mathbb{R}^{N_h}$, via

$$g_h^t[\tau] = \mathcal{M}_{hk}^g X_k^t[\tau] + \mathcal{N}_{hh'}^g H_{h'}^t[\tau-1] + \mathcal{B}_h^g ,$$

where $g = i, f, o, c$ stands for the input, forget, output and cell-state gate, respectively and Eistein's summation convention is employed, i.e. indices that appear twice are summed over. The calligraphic symbols \mathcal{M}_{hk}^g , $\mathcal{N}_{hh'}^g$ and \mathcal{B}_h^g are the free parameters of the network that are optimized for the given problem during the training, which is at the heart of the any machine learning approach. The matrix $\mathcal{M}^g = (\mathcal{M}_{hk}^g) \in \mathbb{R}^{N_h \times N_k}$ can be interpreted as a Markovian-like contribution of the current input $\vec{X}^t[\tau]$ to the gates, whereas the $\mathcal{N}^g = (\mathcal{N}_{hh'}^g) \in \mathbb{R}^{N_h \times N_h}$ scales a non-Markovian part determined by the hidden state of the last sequence point $\tau - 1$. The vector $\mathcal{B}^g = (\mathcal{B}_h^g) \in \mathbb{R}^{N_h}$ is a learnable bias. It should be stressed that these parameters do neither depend on t nor on τ and are thus optimized once for the complete dataset $\{\vec{X}^t\}$.

Note that this mapping is sometimes extended by a contribution to the $g_h^t[\tau]$ from the past cell state $\vec{C}^t[\tau - 1]$ (XXX?). Nevertheless, this mechanism called “peeping” is not further considered in this work.

For the sake of brevity, we write the mapping more compactly in matrix-vector form as

$$\vec{g}^t[\tau] = \mathcal{M}^g \vec{X}^t[\tau] + \mathcal{N}^g \vec{H}^t[\tau - 1] + \vec{\mathcal{B}}^g \quad (1)$$

Second, the actual gate vectors are computed by the core equations of the LSTM as proposed by (XXX?):

$$\begin{aligned} \vec{I}^t[\tau] &= \sigma(\vec{i}^t[\tau]) \\ \vec{F}^t[\tau] &= \sigma(\vec{f}^t[\tau]) \\ \vec{O}^t[\tau] &= \sigma(\vec{o}^t[\tau]) \\ \vec{C}^t[\tau] &= \vec{F}^t[\tau] \circ \vec{C}^t[\tau - 1] + \vec{I}^t[\tau] \circ \tanh(\vec{c}^t[\tau]) \\ \vec{H}^t[\tau] &= \vec{O}^t[\tau] \circ \tanh(\vec{C}^t[\tau]) , \end{aligned} \quad (2)$$

where σ denotes the logistic sigmoid function, \tanh is the hyperbolic tangent and the \circ stands for the Hadamard product (all applied in an element-wise fashion to the vectors). In the last two equations the role of the input, forget and output gates as described above become apparent.

The third step in a single layer LSTM (as employed for the work presented here) is then to provide the output of the current LSTM cell, i.e. $\vec{H}^t[\tau]$ and $\vec{C}^t[\tau]$, to the subsequent LSTM cell that processes the next element $\vec{X}^t[\tau + 1]$ of the input sequence.

The full action of the LSTM network up to the end of the sequence can therefore be written as a nested function call

$$(\vec{H}^t[N_\tau], \vec{C}^t[N_\tau]) = L(\vec{X}^t[N_\tau], L(\vec{X}^t[N_\tau - 1], \dots L(\vec{X}^t[1], (\vec{H}^t[0], \vec{C}^t[0]) \dots)) ,$$

where L represents Eqs. (Equation 1, Equation 2) and the initial conditions are usually chosen as $\vec{H}^t[0] = \vec{C}^t[0] = 0$.

The final output $\vec{H}^t[N_\tau]$ and $\vec{C}^t[N_\tau]$ encode information on the full input sequence ending at time t . This information has to be decoded to obtain useful information via an appropriate subsequent layer, as it is described in the Sec. (XXX?).

A significant advantage of this architecture is the memory cell’s ability to retain gradients. This mechanism addresses the vanishing gradient problem, where, as input sequences elongate, the influence of initial stages becomes harder to capture, causing gradients of early input points to approach zero. The LSTM’s activation function, inherently recurrent, mirrors the identity function with a consistent derivative of 1.0, ensuring the gradient remains stable throughout backpropagation.

2.5 ConvLSTM network

Although the plain LSTM has high performance in handling temporal sequences of point-like quantities it is not designed to recognize spatial features in sequences of two-dimensional maps. To address this limitation we use a convLSTM architecture.

In this kind of network the elements of the input sequence are given as (kind of) vector fields $\vec{X}^t[\tau] = (X_k^t[x, y, \tau]) \in \mathbb{R}^{N_k \times (N_x \times N_y)}$, where $x \in [1, N_x]$ and $y \in [1, N_y]$ run over the horizontal and vertical dimensions of the map, respectively. In order to enable the “learning” of spatial patterns, the free parameters of the network are replaced by two-dimensional convolutional kernels $\mathcal{M}^g = (\mathcal{M}_{hk}^g[\xi, \eta]) \in \mathbb{R}^{(N_h \times N_k) \times (N_\xi \times N_\eta)}$ and $\mathcal{N}^g = (\mathcal{N}_{hh'}^g[\xi, \eta]) \in \mathbb{R}^{(N_h \times N_h) \times (N_\xi \times N_\eta)}$.

163 The width and the height of the kernels are given by N_ξ and N_η , respectively and
 164 $\xi \in [-(N_\xi - 1)/2, (N_\xi - 1)/2]$, $\eta \in [-(N_\eta - 1)/2, (N_\eta - 1)/2]$, where we assume odd
 165 numbers for the kernel sizes.

The mapping from the input quantities to the gates is then given by a convolution
 with these kernels

$$g_h^t[x, y, \tau] = \mathcal{M}_{hk}^g[\xi, \eta] X_k^t[x - \xi, y - \eta, \tau] + \mathcal{N}_{hh'}^g[\xi, \eta] H_{h'}^t[x - \xi, y - \eta, \tau - 1] + \mathcal{B}_h^g[x, y].$$

166 It becomes immediately apparent that in case of the convLSTM, the bias, gate and
 167 state vectors must become vector fields ($\in \mathbb{R}^{N_h \times (N_x \times N_y)}$) as well. We can write this
 168 mapping in the same fashion as Eq. (Equation 1) but with replacing the normal
 169 matrix-vector multiplication by a convolution (denoted with *), i.e.

$$\vec{g}^t[\tau] = \mathcal{M}^g * \vec{X}^t[\tau] + \mathcal{N}^g * \vec{H}^t[\tau - 1] + \vec{\mathcal{B}}^g$$

170 The subsequent processing of the $\vec{g}^t[\tau]$ remains symbolically the same as presented
 171 in Eq. (Equation 2) but with all appearing quantities meaning standing now for
 172 vector fields instead of simple vectors.

173 In summary, the ConvLSTM excels at processing tasks that demand a combined
 174 understanding of spatial patterns and temporal sequences in data. It merges the
 175 image-processing capabilities of Convolutional Neural Networks (CNNs) with the
 176 time-series modeling of Long Short-Term Memory (LSTM) networks.

2.6 Implemented model architecture

177 The ConvLSTM architectures uses an encoder/decoder structure as discussed in
 178 TODO. To predict all 97 rivers entering the Baltic Sea, we flatten the output and
 179 use fully connected layers to map onto the individual rivers outputs.
 180

An overview of the model structure is given below

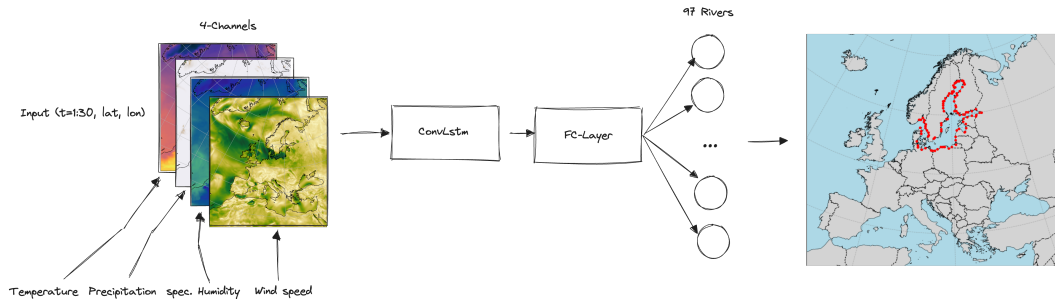


Figure 2: Schematic structure of the convLSTM implementation for river runoff forecasting.

182 For the computation we use the following set of hyper parameters:

Table 1: Hyperparameters

Parameter name	Parameter size
Channel size	4
Num. hidden layer	9
Num. timesteps	30

Parameter name	Parameter size
Conv. Kernelsize	(7,7)
Num. ConvLSTM layers	1
Batch size	50
Learning Rate	1e-3 with CosineAnnealing

183 As input the model receives 30 days of atmospheric surface fields temperature T ,
 184 precipitation P , specific humidity Q and wind speed W , with a daily resolution to
 185 predict the river runoff R at the time step $\Delta t + 1$, which can be summarized as

186
$$R_{\Delta t+1} = f(T_{t-30:t}, P_{t-30:t}, Q_{t-30:t}, W_{t-30:t})$$

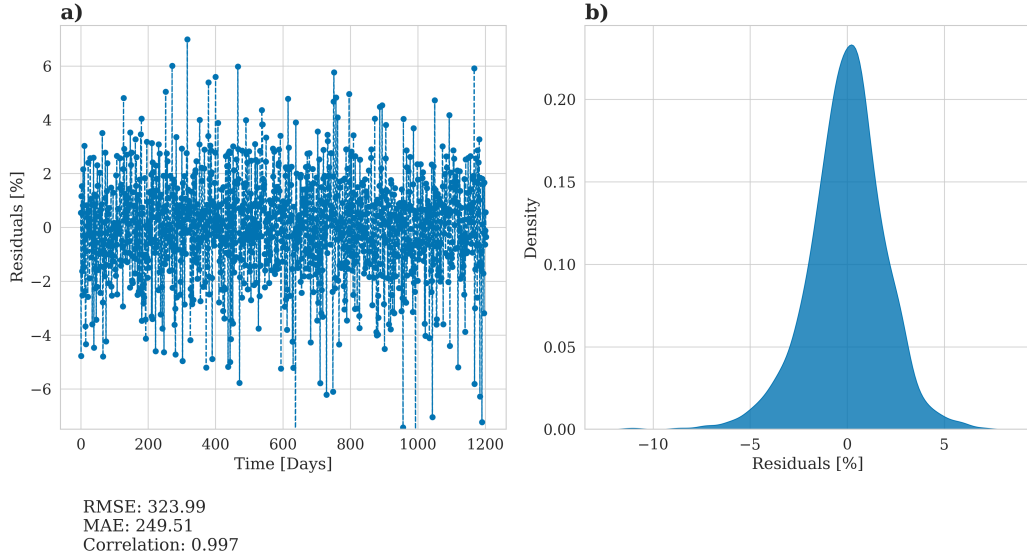
187 with f being a function maps the 30 days of daily atmospheric surface fields data to
 188 the predicted river runoff.

189 The choice of atmospheric fields was based on the implemented river runoff cal-
 190 culation in the atmospheric model COSMO-CLM which uses these four fields to
 191 calculate an river runoff estimate.

192 3 Results

193 The model was trained with daily data for the period 1979 to 2011, as this period
 194 represents the only period of E-HYPE without further bias correction applied to the
 195 runoff to match observations. The data was divided into randomly chosen splits of
 196 80% training data, 10% validation data to evaluate the performance of the model
 197 during training, and 10% training data which is finally used to evaluate the perfor-
 198 mance of the model after training. The model was trained for 400 epochs and the
 199 model weights with the lowest mean squared error during training have been stored.

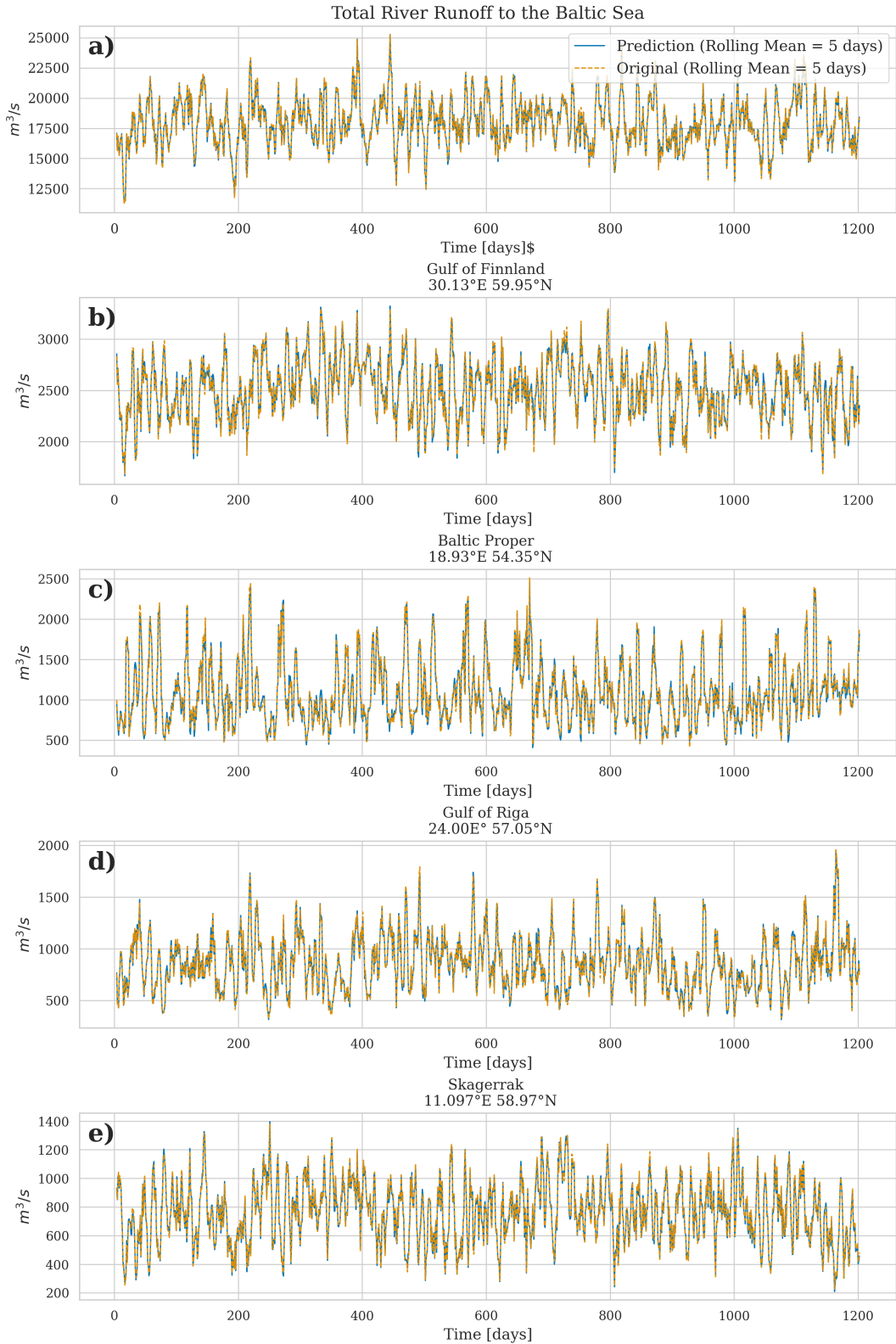
200 The accuracy of the model is displayed in Figure ?@fig-statistical-evaluationNN.
 201 As mention above for evaluation, the test dataset was utilized. The left panel panel
 202 (Figure ?@fig-statistical-evaluationNN a)) illustrates the relative prediction
 203 error in relation to the original E-HYPE data, indicating that, on daily timescales,
 204 the model can predict river runoff with an accuracy of $\pm 5\%$. The overall corre-
 205 lation is 0.997 with the resulting error metrics yielding a RMSE of $323.99 \text{ m}^3/\text{s}$ and
 206 MAE of $249.51 \text{ m}^3/\text{s}$. While the model's performance is satisfactory, the discrep-
 207 ancies between the actual values and the predictions could partly be attributed to
 208 the use of a different atmospheric dataset than the one originally used to drive the
 209 E-HYPE model. However, by applying a rolling mean with a 5-day window, the
 210 prediction error is reduced to less than 1%, which is acceptable for the purposes of
 211 climate modeling. Lastly, the right panel demonstrates that the distribution of resid-
 212 uals follows a Gaussian shape, suggesting that our model does not exhibit bias by
 213 systematically over or underestimating river runoff values.



214

215

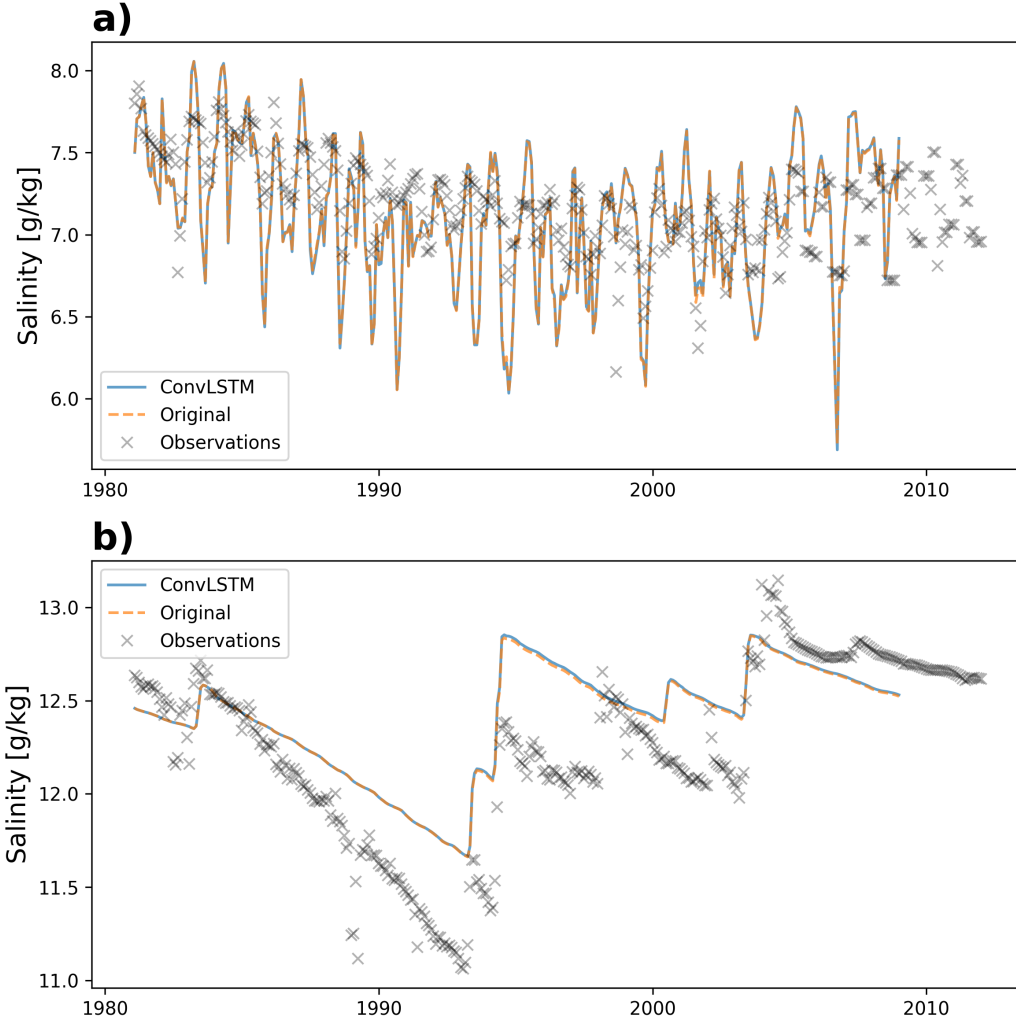
In the following we will now address the overall performance of the total river runoff while also zooming in on the four largest rivers entering the Baltic Sea. @fig-PerformanceNeuralNetworkRunoff shows the predicted and the original river runoff using the test dataset. The predicted total river runoff for the Baltic Sea is closely matching the original data (@fig-PerformanceNeuralNetworkRunoff a). Zooming in on the largest individual rivers (@fig-PerformanceNeuralNetworkRunoff b-e) it can be seen that that also the prediction of the individual rivers is close to the original data.



223

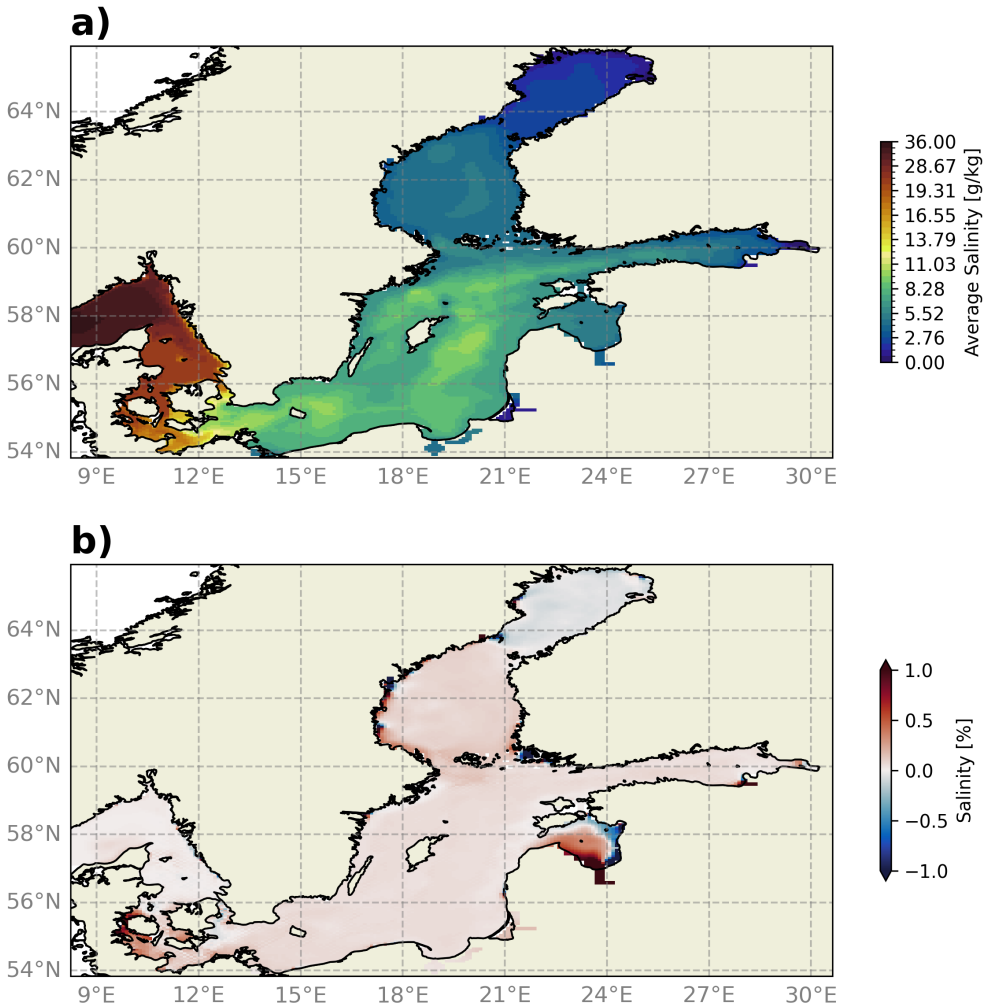
224 Lastly, we evaluated the performance of the runoff model by incorporating the pre-
 225 dicted river runoff as runoff forcing into the ocean model MOM5. This provides a
 226 robust validation of the runoff model against more complex real world conditions.
 227 This allows us to ensure that the predictions accurately reflect the impact of the
 228 river discharge on the ocean dynamics, validating the temporal and spatial variabil-

229
 230
 231
 232
 233
 234
 235
 236
 237
 ity of the the river discharge. ?@fig-by15 shows the salinity comparison between the original E-HYPE river runoff and the predicted river runoff at BY15 - a central stations in the Baltic Sea. It can be seen that the model simulation using the predicted river runoff by the ConvLSTM is closely mirroring the control simulation. The upper panel (?@fig-by15 a) shows the surface salinity, representing the high-frequency variations in the salinity, which is heavily affected by river runoff. The lower panel (?@fig-by15 b) shows the bottom salinity which can be viewed as a low-pass filter in the Baltic Sea, which is also closely mirrored by the ConvLSTM predictions.



238

239
 240
 241
 242
 243
 244
 245
 246
 247
 The final evaluation of the ConvLSTM model concentrates on the spatial accuracy of river runoff predictions. Figure xxx a) shows the vertically averaged salinity for the period 1981 to 2011 in the reference simulation. It highlights the strong horizontal gradients and complex topographic features in the Baltic Sea, as evidenced by salinity variations in deeper waters, captured by the vertical integration. Figure 4b compares these results by showing the percentage difference in vertically averaged salinity between the ConvLSTM simulation and the reference simulation. Overall, the differences remain below 1%, except near a river mouth in the Gulf of Riga (22-24°E, 56.5-58.5°N for orientation), where the difference is approximately 1%.



248

4 Discussion

With the increasing demand of decision makers for regional climate projections, that allow to quantify regional climate change impacts, the availability of precise hydrological forecasting becomes invaluable. The quality of a projection for a coastal sea such as the Baltic Sea is too large parts based on the quality of the hydrological conditions. In this work we analyze the implementation of Convolutional Long Short-Term Memory (ConvLSTM) networks for predicting river runoff, highlighting its potential to enhance river runoff forecasting across different coastal seas. Given the unique hydrological characteristics of the Baltic Sea, largely influenced by its limited connection to the open ocean and significant freshwater input from surrounding rivers, the region presents a critical case for the application of sophisticated forecasting models.

261

The transition from traditional hydrological models to machine learning approaches, such as the ConvLSTM model, offers significant advantages. The ConvLSTM can be seamlessly integrated into regional climate models, allowing for the real-time computation of river runoff while performing climate projections. While the initial training of the model requires substantial computational resources, it remains less intensive than running comprehensive hydrological models. Furthermore, once trained, the ConvLSTM model is computationally efficient during inference, ensuring enhanced forecasting capabilities without significantly increasing computational demands.

While the ConvLSTM represents an advancement for the climate community, given that running and tuning traditional hydrological models demands extensive expertise, models like E-HYPE maintain an essential role. They provide a comprehensive dataset that helps to train our ConvLSTM model effectively. This robust training enables the machine learning models to achieve highly accurate predictive weights. Thus, rather than rendering traditional methods obsolete, the integration of machine learning models builds upon and enhances the foundational data provided by them.

The robust performance of the ConvLSTM model in simulating river runoff and its possible effective integration into regional climate models pave the way for a multitude of new storyline simulations. Hence, we can now explore various “what-if” scenarios more reliably, under the assumption that the model weights attained during training are robust.

In summary, we showed that the ConvLSTM model demonstrated robust performance in forecasting river runoff across 97 rivers entering the Baltic Sea. Trained on data from 1979 to 2011, the model achieved an impressive daily prediction accuracy of $\pm 5\%$. This capability to generate accurate and detailed simulations enables to examine the potential impacts of different climate scenarios. Such precision in forecasting and scenario testing is crucial for crafting effective water resource management strategies and adapting to the changing climate.

Ultimately, the integration of ConvLSTM into regional climate models represents a significant step forward in our ability to understand and predict the complex dynamics of river systems and their impact on regional climate systems.

5 Acknowledgments

Phasellus interdum tincidunt ex, a euismod massa pulvinar at. Ut fringilla ut nisi nec volutpat. Morbi imperdiet congue tincidunt. Vivamus eget rutrum purus. Etiam et pretium justo. Donec et egestas sem. Donec molestie ex sit amet viverra egestas. Nullam justo nulla, fringilla at iaculis in, posuere non mauris. Ut eget imperdiet elit.

6 Open research

Phasellus interdum tincidunt ex, a euismod massa pulvinar at. Ut fringilla ut nisi nec volutpat. Morbi imperdiet congue tincidunt. Vivamus eget rutrum purus. Etiam et pretium justo. Donec et egestas sem. Donec molestie ex sit amet viverra egestas. Nullam justo nulla, fringilla at iaculis in, posuere non mauris. Ut eget imperdiet elit.

References

- Ashrafi, M., Chua, L. H. C., Quek, C., & Qin, X. (2017). A fully-online neuro-fuzzy model for flow forecasting in basins with limited data. *Journal of Hydrology*, 545, 424–435.
- Dee, D. P., Uppala, S. M., Simmons, A. J., Berrisford, P., Poli, P., Kobayashi, S., et al. (2011). The ERA-Interim reanalysis: configuration and performance of the data assimilation system. *Quarterly Journal of the Royal Meteorological Society*, 137(656), 553–597. <https://doi.org/10.1002/qj.828>
- Fang, L., & Shao, D. (2022). Application of long short-term memory (LSTM) on the prediction of rainfall-runoff in karst area. *Frontiers in Physics*, 9, 790687.
- Fang, W., Huang, S., Ren, K., Huang, Q., Huang, G., Cheng, G., & Li, K. (2019). Examining the applicability of different sampling techniques in the development of decomposition-based streamflow forecasting models. *Journal of Hydrology*, 568, 534–550. <https://doi.org/10.1016/j.jhydrol.2018.11.020>
- Gröger, M., Placke, M., Meier, M., Börgel, F., Brunnabend, S.-E., Dutheil, C., et al. (2022). *The Baltic Sea model inter-comparison project BMIP – a platform for model development, evaluation, and uncertainty assessment*. Retrieved from <https://gmd.copernicus.org/preprints/gmd-2022-160/>

- 319 Ha, S., Liu, D., & Mu, L. (2021). Prediction of Yangtze River streamflow based
 320 on deep learning neural network with El Niño–Southern Oscillation. *Scientific
 321 Reports*, 11(1), 11738. <https://doi.org/10.1038/s41598-021-90964-3>
- 322 Hagemann, S., Stacke, T., & Ho-Hagemann, H. T. M. (2020). High Resolution Dis-
 323 charge Simulations Over Europe and the Baltic Sea Catchment. *Frontiers in
 324 Earth Science*, 8. <https://doi.org/10.3389/feart.2020.00012>
- 325 Hochreiter, S., & Schmidhuber, J. (1997). Long short-term memory. *Neural Compu-
 326 tation*, 9(8), 1735–1780.
- 327 Hordoir, R., Axell, L., Höglund, A., Dieterich, C., Fransner, F., Gröger, M., et al.
 328 (2019). Nemo-nordic 1.0: A NEMO-based ocean model for the baltic and north
 329 seas – research and operational applications. *Geoscientific Model Development*,
 330 12(1), 363–386. <https://doi.org/10.5194/gmd-12-363-2019>
- 331 Huang, S., Chang, J., Huang, Q., & Chen, Y. (2014). Monthly streamflow prediction
 332 using modified EMD-based support vector machine. *Journal of Hydrology*, 511,
 333 764–775.
- 334 Humphrey, G. B., Gibbs, M. S., Dandy, G. C., & Maier, H. R. (2016). A hybrid
 335 approach to monthly streamflow forecasting: Integrating hydrological model
 336 outputs into a bayesian artificial neural network. *Journal of Hydrology*, 540,
 337 623–640.
- 338 Kratzert, F., Klotz, D., Brenner, C., Schulz, K., & Herrnegger, M. (2018). Rainfall–
 339 runoff modelling using long short-term memory (LSTM) networks. *Hydrology
 340 and Earth System Sciences*, 22(11), 6005–6022.
- 341 Liu, D., Jiang, W., Mu, L., & Wang, S. (2020). Streamflow prediction using deep
 342 learning neural network: Case study of yangtze river. *IEEE Access*, 8, 90069–
 343 90086.
- 344 Meier, H. M., & Döscher, R. (2002). Simulated water and heat cycles of the baltic
 345 sea using a 3D coupled atmosphere–ice–ocean model. *Boreal Environment Re-
 346 search*, 7(4), 327.
- 347 Moishin, M., Deo, R. C., Prasad, R., Raj, N., & Abdulla, S. (2021). Designing deep-
 348 based learning flood forecast model with ConvLSTM hybrid algorithm. *IEEE
 349 Access*, 9, 50982–50993.
- 350 SHI, X., Chen, Z., Wang, H., Yeung, D.-Y., Wong, W., & WOO, W. (2015). Con-
 351 volutional LSTM Network: A Machine Learning Approach for Precipitation
 352 Nowcasting. In *Advances in Neural Information Processing Systems* (Vol. 28).
 353 Curran Associates, Inc. Retrieved from <https://proceedings.neurips.cc/paper/2015/hash/07563a3fe3bbe7e3ba84431ad9d055af-Abstract.html>
- 355 Tan, Q.-F., Lei, X.-H., Wang, X., Wang, H., Wen, X., Ji, Y., & Kang, A.-Q. (2018).
 356 An adaptive middle and long-term runoff forecast model using EEMD-ANN hy-
 357 brid approach. *Journal of Hydrology*, 567, 767–780. <https://doi.org/10.1016/j.jhydrol.2018.01.015>
- 359 The rossby centre regional climate model RCA3: Model description and perfor-
 360 mance - tellus a: Dynamic meteorology and oceanography. (n.d.). Retrieved
 361 from <https://a.tellusjournals.se/articles/10.1111/j.1600-0870.2010.00478.x>
- 363 Zhu, S., Wei, J., Zhang, H., Xu, Y., & Qin, H. (2023). Spatiotemporal deep learning
 364 rainfall-runoff forecasting combined with remote sensing precipitation products in
 365 large scale basins. *Journal of Hydrology*, 616, 128727.